Composition and temperature-induced structural evolution in La, Sm, and Dy substituted BiFeO$_3$ epitaxial thin films at morphotropic phase boundaries

Daisuke Kan,[1,2,a)] Ching-Jung Cheng,[3] Valanoor Nagarajan,[3,b)] and Ichiro Takeuchi[1]

[1]*Department of Materials Science and Engineering, University of Maryland, College Park, Maryland 20742, USA*
[2]*Institute for Chemical Research, Kyoto University, Gokasyo Uji, Kyoto 611-0011, Japan*
[3]*School of Materials Science and Engineering, University of New South Wales, New South Wales 2052, Australia*

Detailed structural investigations on the substitution-induced structural phase transition from the rhombohedral phase to an orthorhombic phase in (Bi,RE)FeO$_3$ epitaxial thin films (RE = La, Sm, and Dy) grown on (100) SrTiO$_3$ substrates are presented. X ray diffraction reveals that the unit cell dimensions of the orthorhombic phase are strongly dependent on the type of the RE dopant. For RE = La^{3+} ion, which has an ionic size comparable to the Bi^{3+} ion, the unit cell is found to be $a_0 \times a_0 \times 2a_0$, where a_0 is the pseudo-cubic lattice parameter. This is in contrast with the $\sqrt{2}a_0 \times \sqrt{2}a_0 \times 2a_0$ unit cell for the case of smaller ionic radius RE (= Sm and Dy) elements. While clear double-hysteresis loops in the polarization versus electric-field curves due to field-induced transitions are observed for smaller ionic radius RE (= Sm and Dy), no signature of the double hysteresis loops is observed for the RE = La case across the structural boundary. We have also performed systematic tracking of the structural phases as functions of the RE composition and temperature, based on which we propose a phase diagram. This work reveals that the ionic size of the RE element plays a critical role in the evolution of the structural and functional properties of RE-substituted BiFeO$_3$ thin film materials systems. © 2011 American Institute of Physics. [doi:10.1063/1.3605492]

I. INTRODUCTION

Morphotropic phase boundaries (MPBs) in piezoelectric ferroelectric materials are unique compositions where a giant response is observed under an external stimulus, such as electric field or mechanical stress. Composition tuning through A or B site substitution in perovskite ferroelectrics is one well-known route to achieving a MPB behavior.[1–4]

BiFeO$_3$ (BFO) is an environmentally friendly (Pb free) ferroelectric, which also offers the added functionality of room-temperature multiferroelectricity, and chemical substitutions into BFO has been a popular topic of investigation.[5–9] Recently, we discovered[10] a MPB behavior brought about by substitution of a trivalent rare-earth (RE = Sm^{3+}, Gd^{3+}, and Dy^{3+}) into BFO.[11–13] At the MPB, the electromechanical and dielectric properties are substantially enhanced, and the maximum piezoelectric coefficient d_{33} reaches 110 pm/V[14] in epitaxial thin films. We found that the average A-site ionic radius is the universal parameter which determines the structural and ferroelectric properties in RE-BFO.[10] This indicates that the primary cause for the MPB behavior is the chemical pressure effect provided by the RE substitution.

The significance of the chemical pressure effect is confirmed by the observation of lack of enhancement in d_{33} when La^{3+} ions are substituted into BFO.[15] TEM analysis shows that the La^{3+} ion, which is comparable to Bi^{3+} ion in the ionic size, is not able to create the local microstructure closely associated with enhanced electromechanical properties. These results suggest that the substitution-induced structure-functional property correlation evolution depends strongly on the ionic size of the RE^{3+} element.

In this paper, we report details of the substitution and temperature-induced changes in the unit cell size for three typical RE-substituted BFO systems (RE = La^{3+}, Sm^{3+}, and Dy^{3+}). The ionic radii of these trivalent ions, with the coordination number of twelve, are Bi^{3+} (1.36 Å) $\sim$ La^{3+} (1.36 Å) $>$ Sm^{3+} (1.28 Å) $>$ Dy^{3+} (1.24 Å).[16] X ray diffraction reveals that the substitution of the La^{3+} ion results in a structural phase transition from the rhombohedral phase to an orthorhombic phase with the unit cell dimensions of $a_0 \times a_0 \times 2a_0$ (a_0 is the pseudo cubic lattice parameter). In contrast, the smaller RE (= Sm^{3+} and Dy^{3+}) elements result in a phase transition to the orthorhombic phase with unit cell dimensions of $\sqrt{2}a_0 \times \sqrt{2}a_0 \times 2a_0$. It is also found that the structural transition to the $\sqrt{2}a_0 \times \sqrt{2}a_0 \times 2a_0$ orthorhombic phase is accompanied by a distinct decrease by $\sim$0.06 Å in the out-of-plane pseudo-cubic lattice parameter d_{001_pc} (the subscript *pc* denotes the pseudo cubic perovskite notation). A systematic tracking of the changes in structural properties as functions of substitution concentration and temperature allows us to construct a phase diagram that is dependent on the ionic size of the A-site RE element.

a)Author to whom correspondence should be addressed. Electronic mail: dkan@scl.kyoto-u.ac.jp.
b)Electronic mail: nagarajan@unsw.edu.au.

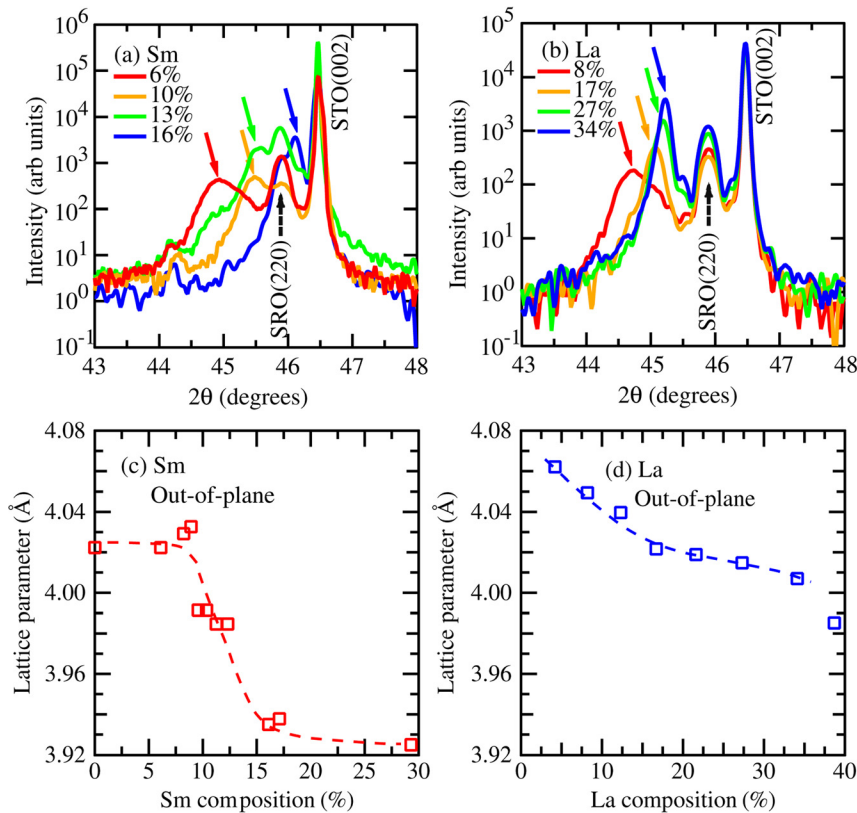FIG. 1. (Color online) (a)-(b) X ray 2θ-θ profiles across the structural phase transition for (a) Sm- and (b) La-substituted BFO thin films. All scans were performed at room temperature. The colored solid arrows denote the $(002)_{PC}$ reflections from RE-substituted BFO layer. (c)-(d) substitution-induced evolution of the out-of-plane lattice parameter d_{001_pc} for (c) Sm- and (d) La-substituted BFO. The lattice parameter is determined from the $(002)_{pc}$ reflection. The dotted line is drawn as a guide to eyes.

II. EXPERIMENTAL DETAILS

200 nm-thick epitaxial $(Bi_{1-x}RE_x)FeO_3$ thin films (RE = La, Sm, and Dy) were fabricated on $SrRuO_3$ (SRO)-buffered (001) $SrTiO_3$ substrates by a pulsed laser deposition (Pascal Inc.). For each RE, a composition spread with gradient from x = 0 to a desired RE concentration (typically, x = 0.3 or larger) was created over a 6 mm length along one direction of the substrate. Sintered ceramic targets of $Bi_{1.1}FeO_3$ and $(RE)FeO_3$ were ablated with an excimer KrF laser with a wavelength of 248 nm (Thin Film Star). During the deposition, temperature and oxygen partial pressure were kept at 600 °C and 25 mTorr, respectively. Compositions were determined by an electron probe (JEOL JXA-8900) within accuracy of ±1%. Crystal structures of the fabricated thin-film composition spreads were characterized by a conventional 4-circle x ray diffractometer and a scanning 2-dimensional x ray diffraction (XRD) (Bruker D8 with GADSS). For electrical characterization, a 100 nm-thick Pd layer was sputtered at room temperature and patterned by a lift-off process into 50 μm by 50 μm top-electrode pads. Polarization versus electric field (P-E) hysteresis loops were measured at 25 kHz with a Radiant Premiere II loop analyzer. The cross-sectional transmission electron microscope (TEM) specimens were prepared by a focused ion beam microscopy (FEI, Nova 200 Nanolab) followed by the "lift-out" technique by a micromanipulator. Selected samples were studied on an *in situ* hot-stage TEM (Philips, CM12) operating at 120 kV. All the electron diffraction patterns were captured at the same exposure time.

III. RESULTS AND DISCUSSIONS

Figures 1(a) and 1(b) display a series of 2θ-θ scans around the (002) STO Bragg reflection across the structural boundary for Sm and La-substituted BFO thin films, respectively. For both cases, only $(002)_{pc}$ reflections from the film and the substrate are seen, confirming epitaxial growth of the RE-BFO film over the substitution composition range studied here. With increasing Sm substitution (Fig. 1(a)), the $(002)_{pc}$ reflection from the Sm-BFO layer shifts toward the higher 2θ side. This change corresponds to the out-of–plane lattice parameter d_{001_pc}, going from 4.02 Å for Sm 6% to 3.98 Å for Sm 13%, as one can see in Fig. 1(c), where d_{001_pc} determined from the $(002)_{pc}$ reflection is plotted as a function of Sm composition. Upon crossing the structural boundary at Sm 14% toward the orthorhombic phase, d_{001_pc} undergoes an abrupt drop by ~0.06 Å (Fig. 1(c)), which corresponds to the observed jump in the $(002)_{pc}$ reflection position for Sm 16% in Fig. 1(a). Once in the orthorhombic phase, d_{001_pc} remains unchanged at ~3.93 Å. Similar results were found for RE = Gd^{3+} and Dy^{3+} (both of which have ionic size smaller than the Sm^{3+} ion), which are in close agreement with our previously reported universality trends.[10]

In sharp contrast, the La-substituted films show a gradual shift of the $(002)_{pc}$ reflections toward the higher 2θ side (Fig. 1(b)) as we increase the La substitution up to La 40%. Correspondingly, we see a gradual decrease in d_{001_pc} from 4.06 Å for 4% to 4.01 Å for 34% in Fig. 1(d), which displays La composition dependence of d_{001_pc}. The observed difference in behavior of d_{001_pc} between RE = La^{3+} and Sm^{3+}
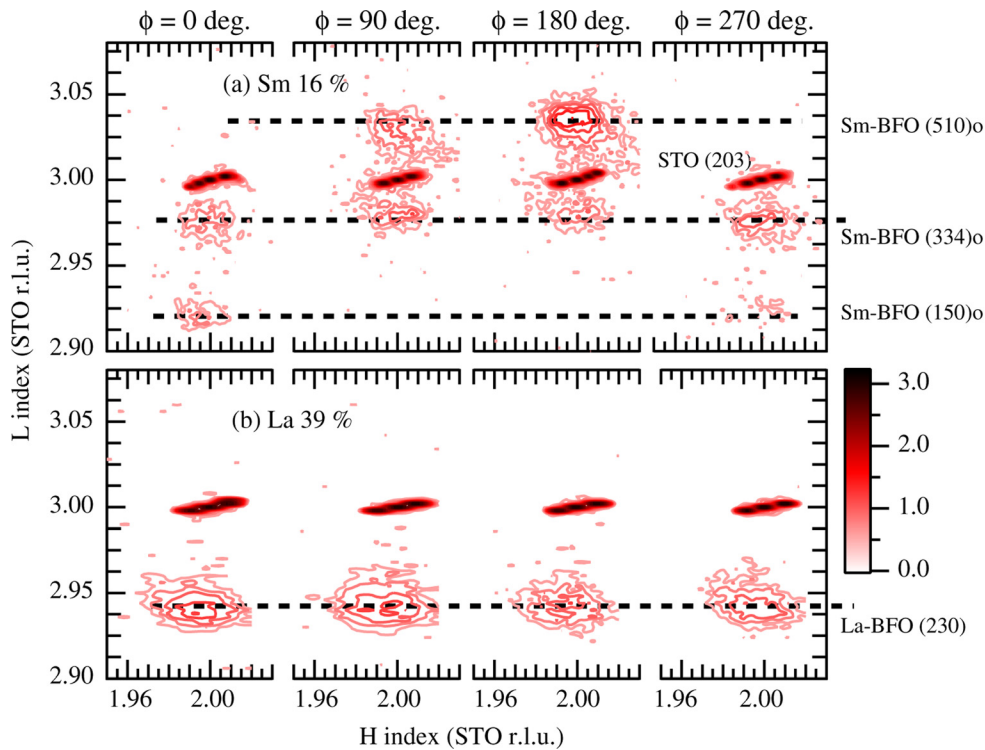
FIG. 2. (Color online) Logarithmic contour plots of reciprocal space mappings taken for the orthorhombic phase in (a) Sm- and (b) La-substituted BFO thin films. The mappings are measured around the (203) SrTiO$_3$ Bragg reflections with phi = 0°, 90°, 180°, and 270° configurations. The intensities are color-coded by the side bar.

already hints at the fact that the substitution-induced evolution from the rhombohedral phase to the orthorhombic one strongly depends on the ionic size of the substitution element and that the orthorhombic phase has a unit cell strongly depending on the ionic size of the RE dopants.

To understand this difference in further detail, x ray reciprocal space mappings (RSMs) around the STO (203)$_{pc}$ Bragg reflection with configurations of phi = 0°, 90°, 180°, and 270° were carried out for RE = Sm and La (Figs. 2(a) and 2(b)). In Fig. 2(a), it is clear that Sm-BFO shows two reflections at each phi configuration. The position of the Sm-BFO (332) reflection remains constant for all four phi configurations (phi = 0°, 90°, 180°, and 270°). However, another diffraction spot corresponding to the (150)$_{Sm-ortho}$ reflection is present at phi configurations of 0° and 270°, while a spot corresponding to the (510)$_{Sm-ortho}$ reflection is only present at phi settings of 90° and 180°. The observed multiple reflections from the Sm-BFO layer suggest that a twin structure is formed in the orthorhombic phase and that the unit cell of the film has the dimensions of $\sqrt{2}a_0 \times \sqrt{2}a_0 \times 2a_0$ with the (110)$_{Sm-ortho}$ orientation. This finding agrees with the obser-

vation of the $1/2(110)_{pc}$ spots from the previous TEM and electron diffraction (ED) studies for RE-BFO (RE = Sm, Gd, and Dy).[12,15] In the case of RE = La, the single reflection from the La-BFO layer is observed, and the reflection appears at the same position for each phi configuration. This implies that the orthorhombic phase for La-BFO has the unit cell dimensions of $a_0 \times a_0 \times 2a_0$ with the (100)$_{La-ortho}$ orientation. This is also consistent with the fact that no $1/2(110)_{pc}$ spot was seen for the orthorhombic La-BFO in an ED study.[10]

The observed RSMs in Figs. 2(a) and 2(b) can be understood by considering the epitaxial relationships drawn in Figs. 3(a) and 3(b) for the RE = Sm and La cases, respectively. Figure 3(a) shows that, due to the dimensions of $\sqrt{2}a_0 \times \sqrt{2}a_0 \times 2a_0$ in Sm-BFO, the film grows with the (110)$_{Sm-ortho}$ orientation on the (001) STO substrate. The epitaxial relationships between the film and the substrate are [001]$_{Sm-ortho}$ // [010]$_{STO}$ and [−110]$_{Sm-ortho}$ // [100]$_{STO}$. Due to the cubic symmetry of the substrate, another relationship, namely [001]$_{Sm-ortho}$ // [100]$_{STO}$ and [−110]$_{Sm-ortho}$ // [010]$_{STO}$, is also allowed. With these epitaxial relationships,
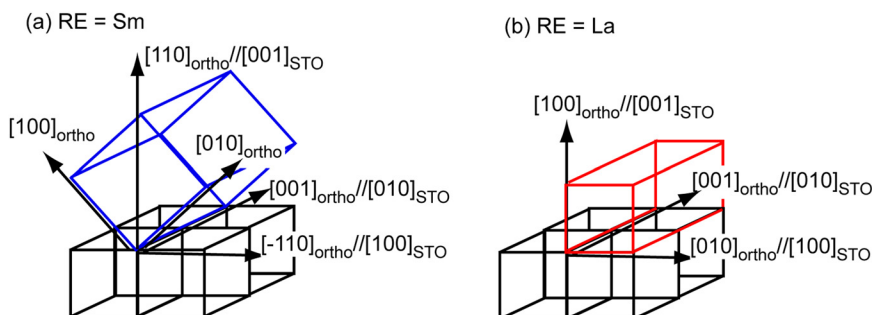

FIG. 3. (Color online) Schematics of the epitaxial relationships between the film and substrate for the orthorhombic phase for RE = Sm (a) and La (b). The cells in black indicate the STO substrate.
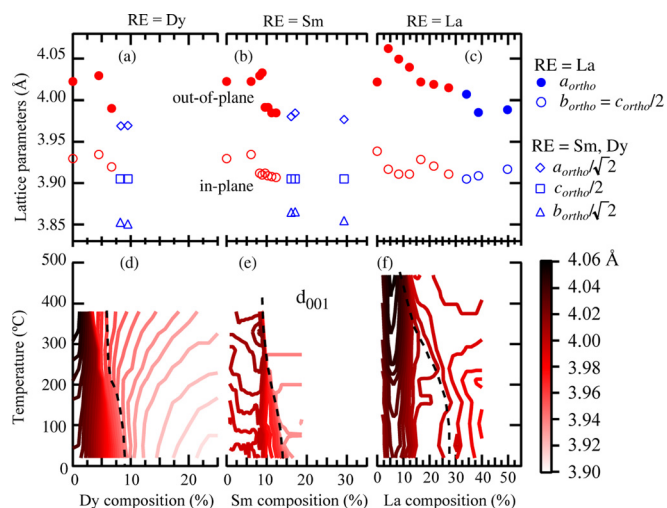
FIG. 4. (Color online) (a)-(c) show evolution in lattice parameters of RE-substituted BFO thin films as a function of the substitution composition. (d)-(f) display contour plots of pseudo-cubic out-of-plane lattice parameters d_{001_pc} as functions of temperature and RE composition. (a) and (d) are for RE = Dy, (b) and (e) for Sm, and (c) and (f) for La, respectively. In (a)-(c), the out-of-plane (filled circle) and in-plane (open circle) lattice parameters for the rhombohedral phase are plotted in red. For the orthorhombic phase, the lattice parameters are colored in blue and are displayed in terms of the pseudo-cubic unit cell. In (d)-(f), the d_{001_pc} is color-coded by the side bar. The black dotted line in the figure denotes the rhombohedral to orthorhombic structural transition boundary, which is determined by the evolution of the $(0, 1/2, 2)$ XRD spot intensity (Fig. 5).

FIG. 5. (Color online) (a)-(c) show room-temperature evolution in normalized intensities of x ray $1/4\{011\}_{pc}$ (squares in red) and $1/2\{010\}_{pc}$ (circles in blue) superstructure reflections of RE-substituted BFO thin films as a function of substitution composition. (d)-(i) display contour plot of x ray superstructure spot intensities as functions of RE ($=$ Dy, Sm, and La) substitution and temperatures. (d)-(f) and (g)-(i) plots the $(0, 1/4, 7/4)$ and $(0, 1/2, 2)$ spot intensities, respectively. (a), (d), and (g) are for RE = Dy. (b), (e), and (h) are for RE = Sm. (c), (f), and (i) are for RE = La. The data in (a) and (b) are taken from Ref. 5. For the contour plots in (d)-(i), the same color-scale on the right is used.

the reflection that appears at the same position in RSMs with all four phi configurations (Fig. 2(a)) is indexed as $(334)_{Sm\text{-}ortho}$. Another reflection observed at two different positions is $(150)_{Sm\text{-}ortho}$ or $(510)_{Sm\text{-}ortho}$. The appearance of these two reflections in the different reciprocal space indicates that the lattice parameter along $[100]_{Sm\text{-}ortho}$ has a different value from the one along $[010]_{Sm\text{-}ortho}$. With the orthorhombic unit cell, the reflection observed for the $2\theta - \theta$ profiles in Fig. 1(a) is assigned as the $(220)_{Sm\text{-}ortho}$ reflection. The abrupt drop in d_{001_pc} observed for RE = Sm (Fig. 1(a)) is attributed to the change in the dimensions of the unit cell, associated with the structural phase transition from the rhombohedral to the orthorhombic phase. Across the boundary, the unit cell volume (in terms of the pseudo-cubic perovskite unit cell) is decreased by 1.2% due to the abrupt drop in d_{001_pc}.

For RE = La, where the unit cell dimensions for the orthorhombic phase is $a_0 \times a_0 \times 2a_0$, the epitaxial relationships are $[100]_{La\text{-}ortho} // [100]_{STO}$, $[010]_{La\text{-}ortho} // [001]_{STO}$, and $[001]_{La\text{-}ortho} // [010]_{STO}$. The cubic symmetry of the substrate results in the crystallographic twin formation allowing another set of relationships, which are $[100]_{La\text{-}ortho} // [010]_{STO}$, $[010]_{La\text{-}ortho} // [001]_{STO}$, and $[001]_{La\text{-}ortho} // [100]_{STO}$. With these relationships, the observed reflection in the RSMs from the La-BFO layer (Fig. 2(b)) is a family of $(230)_{La\text{-}ortho}$ or $(034)_{La\text{-}ortho}$ reflections. The observation of the $\{230\}_{La\text{-}ortho}$ reflections at the same position regardless of the phi configurations clearly indicates that the lattice parameters, d_{010_ortho} and $d_{001\_ortho}/2$, have the same value.
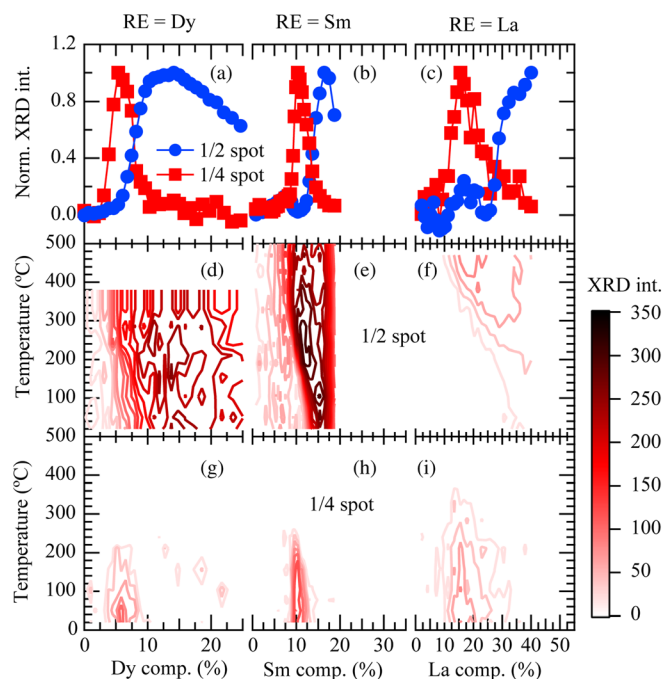
Thus, the fundamental unit-cell for La-BFO (in terms of pseudo-cubic unit cell) remains unchanged across the structural boundary, although the lattice parameter along the $[001]_{ortho}$ axis is doubled, as evidenced by $1/2\{010\}$ XRD spots (see Fig. 5). This also explains why a continuous change in d_{001_pc} is seen only for La-BFO (Fig. 1(b)).

Figures 4(a)–4(c) compares the substitution-induced evolution in lattice parameters at room temperature for the cases of RE = Dy, Sm, and La. For both RE = Dy (Fig. 4(a)) and Sm (Fig. 4(b)), we see a similar trend in the substitution-induced evolution. In the rhombohedral phase (circles in red in Figs. 4(a) and 4(b)), the out-of-plane and in-plane lattice parameters gradually decrease as the substitution is increased. With further substitution, a different set of lattice parameters, a_{orhto}, b_{orhto}, and c_{ortho} (squares, triangles and diamonds in blue in Figs. 4(a) and 4(b)), which correspond to the orthorhombic phase with the unit cell dimensions of $\sqrt{2}a_0 \times \sqrt{2}a_0 \times 2a_0$, are seen. Based on the evolution of the lattice parameters, the composition for the structural transition is determined to be 7% for RE = Dy and 13% for RE = Sm. This is in close agreement with previous analysis performed using changes in the XRD superstructure spots as well as P-E hysteresis loops (see Figs. 5 and 8).[15]

It is found that, as the ionic radius is decreased from Sm^{3+} to Dy^{3+}, the lattice parameters a_{ortho} and b_{ortho} are reduced, while c_{ortho} remains almost unchanged. An important consideration is that, with the relatively smaller ionic

sizes of the Sm^{3+} and Dy^{3+} compared to La^{3+}, one should expect a larger degree of the FeO_6 octahedral rotation around the $[001]_{Sm-ortho}$ direction, according to tolerance factor arguments. In other words, the role of smaller sized RE elements is analogous to a stronger chemical pressure applied to the unit cell. This leads to the larger unit cell dimensions in the orthorhombic phase for the smaller RE substituted BFO, although the pseudo-cubic unit cell becomes smaller with decreasing ionic radius of the RE element, as confirmed by the discontinuous drop in d_{001_pc} in Fig. 1(c).

Based on results of first principles calculations,[10] we had proposed that the enhancement in the out-of-plane piezo-electric coefficient at the structural boundary results from the electric-field-induced structural transformation from the orthorhombic phase to the rhombohedral one at the boundary. The discontinuous change in d_{001_pc} at the structural boundary indicates that there should be a large lattice strain induced by the electric-field-induced structural transformation, and this may be the lattice origin of the enhancement in the piezoelectric coefficient. This model is also supported by the fact that no enhancement is seen for the RE = La case,[10] where there is no obvious discontinuous decease in d_{001_pc} at the structural boundary, as shown in Figs. 1(d) and 4(c). The out-of-plane lattice parameter for La-BFO shows a gradual decrease till 50% substitution, while the in-plane lattice parameter remains almost unchanged. The lack of a distinct change in d_{001_pc} up to La 50% substitution is most likely due to the fact that the primitive unit cell dimensions for La-BFO remains unchanged across the structural boundary.

To further elucidate details in the evolution of the lattice parameters, we investigated temperature dependence of d_{001_pc}. The results are summarized at the lower panel of Fig. 4, where the contour plots of d_{001_pc} for Dy, Sm, and La-substituted BFO as functions of temperature and substitution compositions are displayed with the color-code shown on the right in Fig. 4. The dotted line drawn in Figs. 4(d)–4(f) correspond to the composition where the rhombohedral to orthorhombic structural transition takes place. This boundary is determined by the evolution of the XRD $1/2\{010\}_{pc}$ superstructure spot intensity[10] (Fig. 5), which results from the cell doubling along the $[001]_{Sm-ortho}$ direction in the orthorhombic phase.

For the cases of RE = Dy (Fig. 4(d)) and Sm (Fig. 4(e)), the drop in d_{001_pc} is clearly seen in the entire temperature range as one moves toward higher concentration. The composition where the drop in d_{001_pc} occurs is in very good agreement with the structural boundary (the dotted line in Figs. 4(d)–4(f)), which confirms that this drop results from the structural transition. As temperature is increased, the composition where the drop in d_{001_pc} takes place shifts toward the lower RE substitution level, which implies that the orthorhombic phase is more stable at higher temperatures.

In order to establish a detailed link between the changes in the lattice parameters and the structural phases, we also examined the substitution- and temperature-induced evolution of the XRD superstructure spot intensities. In our previous report,[17] we demonstrated that the structural evolution from the rhombohedral to orthorhombic phase in the smaller RE-substituted BFO (RE = Dy, Gd, and Sm) can be directly linked to changes in the XRD $1/4\{110\}_{pc}$ (referred to as the $1/4$ spot) and $1/2\{010\}_{pc}$ (referred to as the $1/2$ spot) super-structure spot intensities. Based on the TEM and electron diffraction (ED) studies,[18,19] it was determined that the $1/4$ spot arises from the presence of minority phase with a $PbZrO_3$-type structure[5,17] with dimensions of $\sqrt{2}a_0 \times 2\sqrt{2}a_0 \times 2a_0$ in local regions and that the $1/2$ spot results from the cell-doubled orthorhombic structural phase. As one increases the RE substitution concentration, at first, the $1/4$ spot begins to appear and is found to have a maximum intensity before the structural boundary. With further substitution, the $1/4$ spot disappears while the $1/2$ spot becomes more prominent. The structural phase boundary corresponds to the composition where the normalized intensities of $1/4$ and $1/2$ spots switch over as the $1/2$ spot arises from the cell doubling along the $[010]_{pc}$ direction. In Figs. 5(a) and 5(b), we plot the room-temperature RE composition dependence of the normalized intensities of the $1/4$ and $1/2$ spots for Dy- and Sm-BFO, respectively. For La-BFO in Fig. 5(c), the trend is similar to the Dy and Sm cases, indicating that the occurrence of $1/4$ and $1/2$ spots are indeed universal characteristics for RE-BFO.

Figures 5(d)–5(i) display the contour plots of the $1/2$ (Figs. 5(d)–5(f)) and $1/4$ spot intensities (Figs. 5(g)–5(i)) as functions of temperature and the substitution concentration for the RE = Dy, Sm, and La cases. The intensities in Figs. 5(d)–5(i) are plotted in the same color-code on the right in the figure. Again, we find a universal trend in the temperature-induced variation in $1/4$ and $1/2$ spot intensities. As temperature is increased, the composition space where the $1/4$ spot is stable shrinks and eventually disappears. Concurrently, the $1/2$ spot begins to become more pronounced. By comparing Fig. 5 to Fig. 4 for RE = Dy and Sm cases, it is clear that the composition region where the $1/4$ and $1/2$ spot intensities switch over coincides very well with the composition region in which the discontinuous drop in d_{001_pc} is seen. More importantly, the stability of the structural phase shows a strong correlation to the strength of the chemical pressure due to the substitution. As the chemical pressure gets stronger, the highest temperature at which the $1/4$ spot appears decreases from 360 °C for RE = La to 200 °C for RE = Dy, although the overall spot intensity is smaller for the La case. The stronger pressure also moves the $1/4$ spot region into the lower composition side. In the same vein, the composition region where the $1/2$ spot intensity is seen is extended toward lower composition and lower temperature region with decreasing ionic size of the RE elements.

It is interesting to note that, in the contour plots for RE = Dy (Fig. 4(d)) and Sm (Fig. 4(e)), we see another slight decrease of d_{001_pc} by ≈ 0.03 Å in the composition region right before the structural transition (on the rhombohedral phase side). This composition region becomes narrower with increasing temperature and disappears above $\sim$200 °C. This behavior strongly resembles the temperature-induced evolution of the XRD $1/4\{011\}_{pc}$ superstructure spot intensity in Fig. 5, suggesting a close tie between the slight decrease in d_{001_pc} and the appearance of the $1/4$ structural phase. However, further examination is necessary to identify an underlying origin of the slight decrease in d_{001_pc} in this
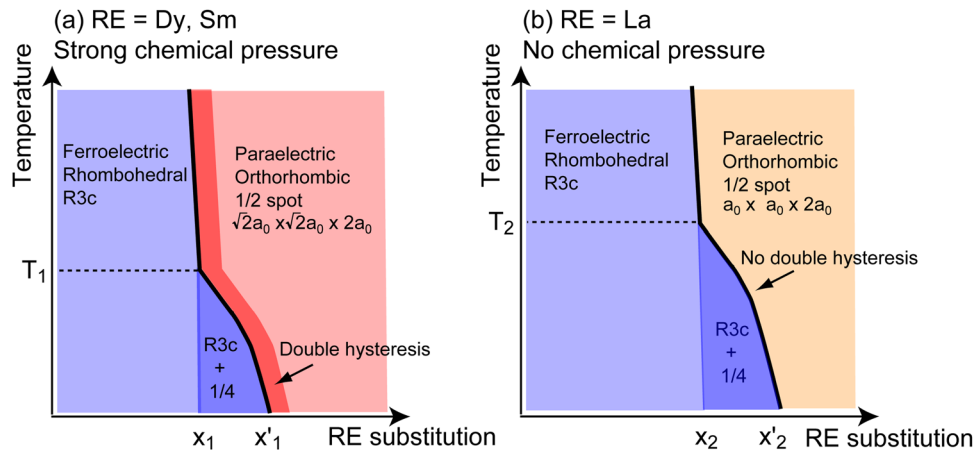
FIG. 6. (Color online) Schematic phase diagram for RE-substituted BFO in presence of (a) the strong chemical pressure due to RE substitutions (RE = Dy and Sm) and (b) no (or negligibly weak) chemical pressure (RE = La). The subscripts 1 and 2 denote for the strong chemical pressure case (RE = Sm and Dy) and no chemical pressure case (RE = La), respectively. In the diagram, T_1 and T_2 denote the highest temperature at which the $1/4$ spot appears. x_1 and x'_1 (x_2 and x'_2 for the RE = La case) stand for the compositions at which the $1/4$ spot appears and disappears at room temperature. The stronger chemical pressure shifts the $1/4$ spot region into lower temperature and lower composition side ($T_1 < T_2$, $x_1 < x_2$, $x'_1 < x'_2$).

composition region. For the RE = La case, this behavior in d_{001_pc} is not obvious. This is probably due to the negligibly weak chemical pressure effect for the La substitution, resulting in the continuous decrease in d_{001_pc}.

Figure 6 summarizes the structural evolution in RE-substituted BFO. Figure 6(a) depicts the schematic phase diagram for the case of smaller RE ionic sizes (the strong chemical pressure) that can stabilize the $1/2$ structural phase with dimensions of $\sqrt{2}a_0 \times \sqrt{2}a_0 \times 2a_0$. We define X and X' as a substitution composition at which the $1/4$ and $1/2$ spot intensities begin to appear at room temperature, respectively. (The subscripts 1 and 2 in Figure 6 denote the strong chemical pressure case (RE = Sm and Dy) and the no chemical pressure case (RE = La), respectively.) For lower temperatures, the appearance of the $1/4$ phase (in the composition region between X and X' at room temperature) seemingly "bridges" the rhombohedral structural phase to the orthorhombic phase. The orthorhombic phase emerges in the composition region beyond X' at room temperature. As temperature is increased, the $1/4$ spot disappears, and the orthorhombic phase is located right next to the rhombohedral phase in the diagram.

Based on the observations in Figs. 4 and 5, this phase diagram in Fig. 6(a) can be extended to the case where the chemical pressure effect is negligibly weak (RE = La) by simply shifting the $1/4$ spot region and the structural boundary into the higher substitution composition and higher temperature regions. In this case, the $1/2$ structural phase is the orthorhombic (or tetragonal-like) phase with dimensions of $a_0 \times a_0 \times 2a_0$, although the $1/2$ structural phase is still bridged by the $1/4$ phase to the rhombohedral phase at lower temperatures. In the higher temperature region, where the $1/4$ spot disappears, the $1/2$ phase remains right adjacent to the rhombohedral phase in the diagram.

To confirm microscopically the phase diagram presented in Fig. 6, we have studied temperature dependence of ED spots observed for the $1/4$ phase in a local region at the composition of $Bi_{0.9}Sm_{0.1}FeO_3$. Previously, we discussed that

the regions, which show $1/4\{110\}$ spots are nanoscale (10-20 nm) pockets in the rhombohedral ferroelectric matrix.[10,18] Fig. 7 displays the ED patterns taken for the local $1/4$ structural phase for $Bi_{0.9}Sm_{0.1}FeO_3$ as a function of temperature. The $1/4\{110\}$ spot (circled in red), captured for one such pocket at room temperature in Fig. 7(a), disappears as one raises the temperature. Subsequently, the $1/2\{010\}$ spots appear (boxed in blue) and remain with further increase in temperature up to 130 °C (Fig. 7(d)). Figure 7 thus confirms that the local regions with the $1/4\{110\}$ spots undergo a structural transition to an orthorhombic structural phase that is identical to the majority phase. It should be noted that the orthorhombic phase is a *single global phase* without any minority phases. The general trend of the $1/4$ to $1/2$ structural phase transition, seen as a function of temperature in Fig. 7, is consistent with the results shown in Figs. 5 and 6.
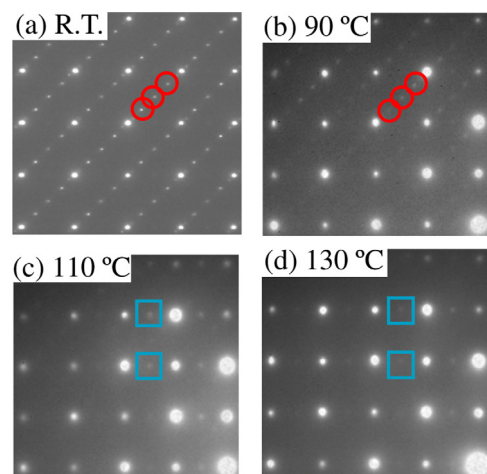

FIG. 7. (Color online) Temperature dependence of electron diffraction patterns for the local $1/4$ structural phase in $Bi_{0.9}Sm_{0.1}FeO_3$ thin films. The patterns were taken at (a) room temperature, (b) 90 °C, (c) 110 °C, and (d) 130 °C. The $1/4\{110\}_{pc}$ and $1/2\{010\}_{pc}$ spots are denoted by red circles and blue boxes, respectively.
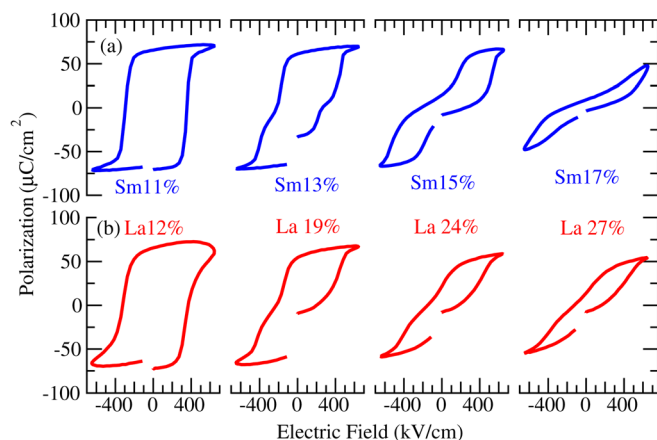
FIG. 8. (Color online) Evolution in the room temperature P-E hysteresis loops across the structural transition for Sm- (upper panels) and La-substituted BFO thin films (lower panels). All loops were acquired at 25 kHz.

As an important consequence of the substitution-induced structural evolution, ferroelectric properties of the RE-BFO thin films display concomitant changes, which exhibit strong dependence on the degree of the chemical pressure due to the RE elements. Figure 8 displays the evolution of room-temperature P-E hysteresis loops across the structural boundary for Sm- and La-BFO thin films. The compositions for RE = Sm and La cases are chosen such that they capture the representative characteristics of the evolution in sufficient composition ranges. For RE = Sm in Fig. 8(a), the P-E hysteresis loop undergoes a transition from the ferroelectric single loop on the rhombohedral phase side into the double-hysteresis one on the orthorhombic phase. Results from a first principles calculation have been used[15] to propose that the origin of the double hysteresis loops is the electric-field induced structural transformation from the paraelectric orthorhombic phase to a ferroelectric rhombohedral phase. As one approaches the structural phase boundary, a ferroelectric single hysteresis loop with the saturated polarization of 70 $\mu C/cm^2$ first becomes distorted and then fully develops into the double-hysteresis loop. The similar trend is seen for the La case except the orthorhombic phase, as exemplified by the loop for La 27%, where the double hysteresis behavior becomes less pronounced and the P-E loop is likely the one characteristic for the paraelectric phase. This behavior of La-substituted BFO is independently confirmed by the

dielectric constant versus electric field curves,[15] which did not show clear quadruple-humped loops observed for the orthorhombic phase adjacent to the boundary in Sm-substituted BFO.

Figure 9 shows the P-E hysteresis loops observed for the Sm 18% and La 34% substituted BFO thin films with the orthorhombic structural phase. Both films show the P-E hysteresis loops characteristic for the paraelectric phase when the applied electric field is below 500 kV/cm. As we increase the applied electric fields further, the Sm-BFO shows the recovery of the well-developed double hysteresis behavior while the paraelectric behavior remains unchanged for the RE = La case. Similar behaviors are observed for the orthorhombic phase with other La substitution composition close to the structural boundary. Based on the fact that the unit cell dimensions of the orthorhombic phase is different for RE = La compared to BFO substituted with smaller RE elements, we conclude that the electric-field induced structural transformation is only favorable for the orthorhombic phase with $\sqrt{2}a_0 \times \sqrt{2}a_0 \times 2a_0$ dimensions.

IV. SUMMARY

We have investigated in detail the structural phase transitions in La, Sm, and Dy-substituted BFO thin films as a function temperature and composition space. The common structural transition from the rhombohedral to an orthorhombic phase is observed for all RE elements. However, we find that the orthorhombic phase beyond the structural boundary has the unit cell dimensions that strongly depend on the type of the RE element. In the case of La^{3+}, which has the same ionic radius as the Bi^{3+} ion, the orthorhombic phase has the dimensions of $a_0 \times a_0 \times 2a_0$, as compared to the $\sqrt{2}a_0 \times \sqrt{2}a_0 \times 2a_0$ orthorhombic unit cell for the smaller RE cases, such as Sm and Dy. We attribute this to the greater degree of instability of the perovskite structure and, hence, the rotation of the FeO_6 octahedron for the smaller RE cases. This leads to larger dimensions in the orthorhombic phase for the smaller RE substituted BFO, which consequently exhibits an abrupt drop in the pseudo-cubic out-of-plane lattice parameter. In contrast, the La-substituted BFO shows a smooth change in the out-of-plane lattice parameter. Based on the substitution- and temperature-induced evolution of the lattice parameters and XRD superstructure spots, we also
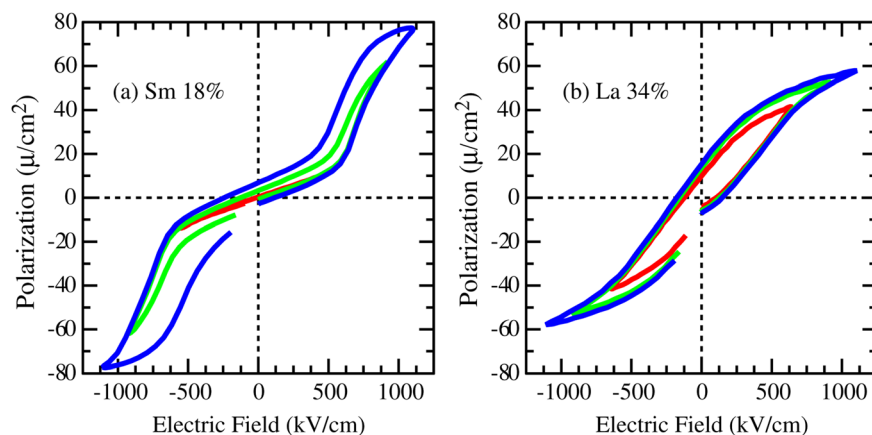

FIG. 9. (Color online) Room-temperature P-E hysteresis loops observed for the orthorhombic structural phase in Sm 18% and La 34% substituted BFO thin films. All loops were acquired at 25 kHz.

established the phase diagrams for cases of the strong (RE = Sm and Dy) and negligibly weak chemical pressure (RE = La) into the BFO lattice.

The phase diagrams reveal the great impact of the chemical pressure effect on the stability of the orthorhombic structural phase of RE-substituted BFO in the composition and temperature space. The RE-BFO displays the concomitant changes in ferroelectric properties across the structural phase transition. For the RE = La case, no signature of the double P-E hysteresis loop is observed across the boundary, while the smaller RE substituted BFO shows fully developed double hysteresis loops. These results underscore the fact that subtle change in the degree of chemical pressure effect provided by substitution of different RE elements has profound influences on structural and ferroelectric properties of RE-substituted BFO.

ACKNOWLEDGMENTS

[1]S.-E. Park and T. R. Shrout, J. Appl. Phys. **82**, 1804 (1997).

[2]R. Guo, L. E. Cross, S.-E. Park, B. Noheda, D. E. Cox, and G. Shirane, Phys. Rev. Lett. **84**, 5423 (2000).

[3]Z. Kutnjak, J. Petzelt, and R. Blinc, Nature **441**, 956 (2006).

[4]Y. Saito, H. Takao, T. Tani, T. Nonoyama, K. Takatori, T. Homma, T. Nagaya, and M. Nakamura, Nature **432**, 84 (2004).

[5]S. Karimi, I. M. Reaney, I. Levin, and I. Sterianou, Appl. Phys. Lett. **94**, 112903 (2009).

[6]I. O. Troyanchuk, D. V. Karpinsky, M. V. Bushinsky, V. A. Khomchenko, G. N. Kakazei, J. P. Araujo, M. Tovar, V. Sikolenko, V. Efimov, and A. L. Kholkin, Phys. Rev. B **83**, 054109 (2011).

[7]D. A. Rusakov, A. M. Abakumov, K. Yamaura, A. A. Belik, G. V. Tendeloo, and E. Takayama-Muromachi, Chem. Mater. **23**, 285 (2011).

[8]G. L. Yuan and S. W. Or, J. Appl. Phys. **100**, 024109 (2006).

[9]Y. H. Chu, Q. Zhan, C.-H. Yang, M. P. Cruz, L. W. Martin, T. Zhao, P. Yu, R. Ramesh, P. T. Joseph, I. N. Lin, W. Tian, and D. G. Schlom, Appl. Phys. Lett. **92**, 102909 (2008).

[10]D. Kan, L. Palova, V. Anbusathaiah, C. J. Cheng, S. Fujino, V. Nagarajan, K. M. Rabe, and I. Takeuchi, Adv. Funct. Mater. **20**, 1108 (2010).

[11]G. Catalan and J. F. Scott, Adv. Mater. **21**, 2463 (2009).

[12]J. Wang, J. B. Neaton, H. Zheng, V. Nagarajan, S. B. Ogale, B. Liu, D. Viehland, V. Vaithyanathan, D. G. Schlom, U. V. Waghmare, N. A. Spaldin, K. M. Rabe, M. Wuttig, and R. Ramesh, Science **299**, 1719 (2003).

[13]T. Zhao, A. Scholl, F. Zavaliche, K. Lee, M. Barry, A. Doran, M. P. Cruz, Y. H. Chu, C. Ederer, N. A. Spaldin, R. R. Das, D. M. Kim, S. H. Baek, C. B. Eom, and R. Ramesh, Nature Mater. **5**, 823 (2006).

[14]S. Fujino, M. Murakami, V. Anbusathaiah, S.-H. Lim, V. Nagarajan, C. J. Fennie, M. Wuttig, L. Salamanca-Riba, and I. Takeuchi, Appl. Phys. Lett. **92**, 202904 (2008).

[15]C.-J. Cheng, D. Kan, V. Anbusathaiah, I. Takeuchi, and V. Nagarajan, Appl. Phys. Lett. **97**, 212905 (2010).

[16]Y. Q. Jia, J. Solid State Chem. **95**, 184 (1991).

[17]C.-J. Cheng, D. Kan, S.-H. Lim, W. R. McKenzie, P. R. Munroe, L. G. Salamanca-Riba, R. L. Withers, I. Takeuchi, and V. Nagarajan, Phys. Rev. B **80**, 014109 (2009).

[18]C.-J. Cheng, A. Y. Borisevich, D. Kan, I. Takeuchi, and V. Nagarajan, Chem. Mater. **22**, 2588 (2010).

[19]E. Sawaguchi, H. Maniwa, and S. Hoshino, Phys. Rev. **83**, 1078 (1951).